



Cite this: *RSC Adv.*, 2024, 14, 2214

# Facile synthesis of $\text{NiFe}_2\text{O}_4$ -based nanoblocks for low-temperature detection of trace *n*-butanol

Xiujuan Qian, Yanping Chen, \* Yuye Tao, Jian Zhang, Guangfeng Zhang and Haoyang Xu

$\text{Fe}_2\text{O}_3$ -loaded  $\text{NiFe}_2\text{O}_4$  nanoblocks were successfully developed under a straightforward one-step hydrothermal synthesis method, aiming to detect trace amounts of *n*-butanol at the parts per billion (ppb) concentration range. The synthesized samples were comprehensively characterized using various techniques, including XRD, SEM, XPS, TEM and SAED. At a tantalizingly low temperature of 130 °C, the Ni/Fe-2 gas sensor demonstrated the optimum response ( $R_a/R_g = 29.747$  @ 10 ppm) to *n*-butanol. Furthermore, Ni/Fe-2 sensor exhibited remarkable stability and reproducibility and an ultra-low detection limit. The enhanced gas sensitivity was primarily due to the assembly of Ni/Fe-2 nanoblocks from differently sized nanospheres, which exhibited a rich surface porosity conducive to gas adsorption. Besides, the formation of heterojunctions and the augmentation of oxygen vacancy content are also conducive to enhancing gas sensing capabilities. The Ni/Fe-2 sensor is expected to successfully detect trace amounts of *n*-butanol.

Received 25th October 2023  
Accepted 13th December 2023

DOI: 10.1039/d3ra07264a

rsc.li/rsc-advances

## 1 Introduction

*N*-butanol is commonly utilized as an industrial chemical and cleaning agent.<sup>1,2</sup> Nevertheless, protracted contact with it may inflict harm upon human well-being and lead to a cascade of discomforting symptoms, such as headaches, dizziness, nausea, vomiting and diarrhea.<sup>3</sup> Furthermore, *n*-butanol can pollute water and soil, thereby compromising the health of the ecological environment. Therefore, the development of extremely sensitive gas sensors in factories and laboratories is considerably imperative to monitor the *n*-butanol gas concentration.<sup>4</sup>

Metal oxide semiconductor (MOS) gas sensors are widely used in industrial applications and household settings because of their benefits, including straightforward operation processes and real-time monitoring capabilities.<sup>5</sup> The  $\text{NiFe}_2\text{O}_4$  gas sensors have received significant attention in recent years. The structure exhibits a classic inverse spinel arrangement, with  $\text{Ni}^{2+}$  ions occupying the octahedral site and  $\text{Fe}^{3+}$  ions filling the tetrahedral site. The presence of  $\text{Ni}^{3+}/\text{Ni}^{2+}$  and  $\text{Fe}^{3+}/\text{Fe}^{2+}$  ions existing in  $\text{NiFe}_2\text{O}_4$  leads to an increased carrier concentration, which manifests its great potential for development as a sensing material with high sensitivity. For instance, Pan *et al.*<sup>6</sup> reported that a unique heterostructure of NiO nanoprisms modified  $\text{Fe}_2\text{O}_3$  nanosheets to detect *n*-butanol concentration. Gas-sensing experiments demonstrated that the NiO/ $\text{Fe}_2\text{O}_3$  sensor has an impressive response value of 4.2 ( $S = R_a/R_g$ ) at 200 °C for

10 ppm *n*-butanol. Furthermore, the sensor demonstrates a minimum detectable concentration (48 ppb). The improved sensitivity results from the regulation of electron transport through p–n heterostructure, along with the increased specific surface area and adsorbed oxygen level. Zhang *et al.*<sup>7</sup> successfully synthesized  $\text{NiFe}_2\text{O}_4$  nanorods to detect toluene, which displayed the greatest sensitivity ( $R_a/R_g = 59.64$  @ 500 ppm) when worked at 200 °C. The catalytic activity, large surface area, and porous structures of  $\text{NiFe}_2\text{O}_4$  nanorods render it suitable for toluene detection. Liu *et al.*<sup>8</sup> presented  $\text{NiFe}_2\text{O}_4$  nanoboxes with a porous hollow structure prepared through annealing the self-sacrificed templates of hydrothermally synthesized metal–organic frameworks (MOFs) for the detection of ethyl acetate, which showed a high response value at 64.27 ( $S = R_a/R_g$ ) to 200 ppm EtOAc at 120 °C. Additionally, the sensor based on  $\text{NiFe}_2\text{O}_4$  exhibited a detection limit (LOD) of approximately 0.26 ppm. The unique porous hollow morphology and multiple surface element states result in excellent gas-sensitive performance. Based on the aforementioned analysis, it is evident that the majority of  $\text{NiFe}_2\text{O}_4$  sensors are constrained by elevated operating temperatures. Additionally, the sensitivity of sensors also needs to be further improved to meet the demand for detecting low-concentration gases. Consequently, additional research is required to decrease sensors operating temperatures, enhance response speed and improve sensitivity.

In this work, the  $\text{Fe}_2\text{O}_3$ -loaded  $\text{NiFe}_2\text{O}_4$  nanoblocks were successfully generated to realize the determination of low concentrations of *n*-butanol gas at ppb level. Ni/Fe-2 gas sensor was evidenced the most outstanding response ( $R_a/R_g = 29.747$  @ 10 ppm) to *n*-butanol at 130 °C. The SEM images revealed

School of Science, Shandong Jianzhu University, Jinan 250100, China. E-mail: yanping\_c@sdjzu.edu.cn



that the prepared sample was composed of nanoblocks formed by the aggregation of nanospheres, and the abundant porosity may result in high response. Furthermore, the Ni/Fe-2 gas sensor exhibited an ultra-low limit. Therefore, it is reasonable to propose that the Ni/Fe-2 gas sensor has significant importance for the measurement of *n*-butanol gas.

## 2 Experimental

### 2.1 Materials

Iron nitrate nonahydrate ( $\text{Fe}(\text{NO}_3)_3 \cdot 9\text{H}_2\text{O}$ ), nickel acetate tetrahydrate ( $\text{Ni}(\text{CH}_3\text{COO})_2 \cdot 4\text{H}_2\text{O}$ ), polyvinyl pyrrolidone (PVP), sodium hydroxide (NaOH), *N,N*-dimethylformamide (DMF), and other chemicals were procured from Sinopharm Chemical Reagent Co. Ltd. These analytical-grade reagents do not require any additional purification steps during the material preparation process.

### 2.2 Preparation of $\text{NiFe}_2\text{O}_4$ composites with varying Ni/Fe atomic ratios

The synthesized  $\text{NiFe}_2\text{O}_4$ -based nanoblocks with varying Ni/Fe atomic ratios were obtained using the hydrothermal method. As illustrated in Fig. 1(a), solution A was prepared by dissolving 0.025 mol of  $\text{Fe}(\text{NO}_3)_3 \cdot 9\text{H}_2\text{O}$  and the specified dosage of  $\text{Ni}(\text{CH}_3\text{COO})_2 \cdot 4\text{H}_2\text{O}$  in 60 mL of deionized water (DIW), followed by thorough stirring to obtain a brown-black solution. Concurrently, 60 mL of DMF were mixed briskly with 5.7 g of PVP to prepare a semi-transparent solution B. Afterward, solution B was gradually mixed with the previous solution with continuous stirring, while an appropriate amount of NaOH solution was poured into above solution until no new precipitate formed. After 5 minutes of sonication, the resultant precursor solution was put in an autoclave which was kept at 150 °C for a duration of 12 hours. The obtained precipitate

underwent centrifugation, washing, and was dried overnight in a water bath at a temperature of 60 °C. Finally, the materials annealed at 500 °C for 2 h ( $5\text{ °C min}^{-1}$ ) to obtain the brown powders.

The obtained samples were named Ni/Fe-*x* (*x* = 1, 2, 4, 6, 8, 10), according to the different Ni/Fe atomic ratios of 1 : 10, 2 : 10, 4 : 10, 6 : 10, 8 : 10 and 10 : 10, respectively.

### 2.3 Gas sensitivity test

A slight quantity of the acquired powder samples was blended with a suitable quantity of DIW in a mortar to grind into a paste. The paste obtained was subsequently spread onto the ceramic tube surface to produce a sensing film measuring approximately 0.1 mm in thickness. As shown in Fig. 1(b), a brace of golden electrodes and four platinum wires were pre-deposited at both ends of the ceramic tube. The nickel-chromium coil traversed through the ceramic tube for temperature regulation of the sensor. Gas-sensitive performance was assessed using WS-30A (Zhengzhou Weisheng Technology Co., Ltd., China) after 48 h of aging on the aging platform. During the entire gas sensing experiment, target gases of various concentrations were prepared *via* the static thermal evaporation method. As illustrated in Fig. 1(c), a micro-syringe was utilized to extract the necessary amount of liquid reagent. Subsequently, the reagent was injected onto the evaporation plate within the test apparatus. The volume of reagent required for the target concentration<sup>9</sup> can be obtained by applying eqn (1):

$$C = \frac{22.4 \times \omega \times \rho \times V_1}{M \times V_2} \quad (1)$$

in which *C* (ppm) represents the concentration of tested gases,  $\omega$  denotes the reagent mass percentage,  $\rho$  ( $\text{g mL}^{-1}$ ) represents the reagent density,  $V_1$  ( $\mu\text{L}$ ) represents the reagent volume, *M* (g

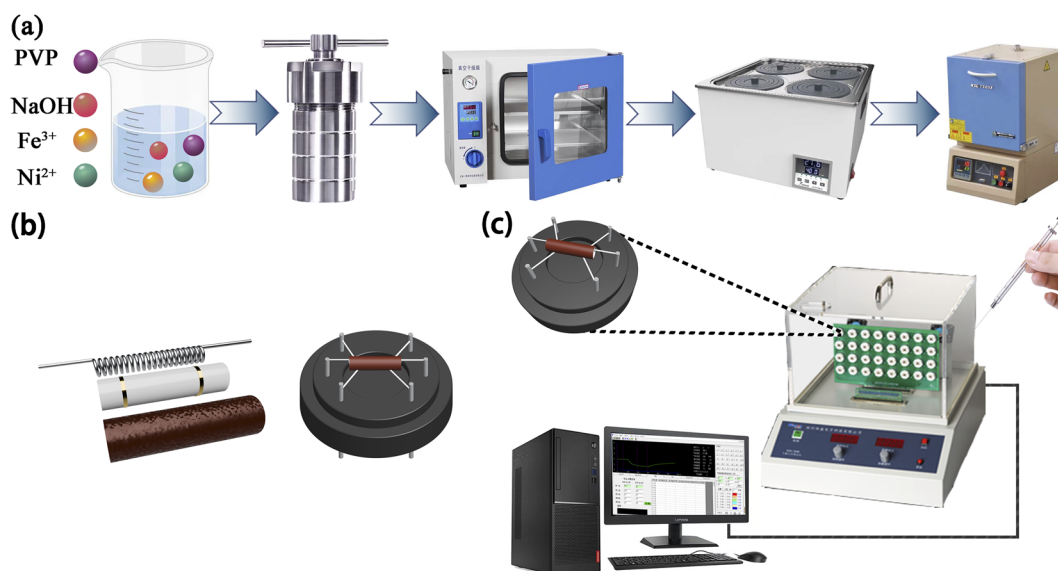


Fig. 1 (a) Process flow chart of preparing Ni/Fe composite nanomaterials. (b) Composition diagram of gas sensor. (c) Gas sensitivity detection equipment.



$\text{mol}^{-1}$ ) denotes the reagent molecular weight, and  $V_2$  (L) represents the test chamber volume.<sup>10</sup>

During the detection of gases with reducing properties, the gas sensor's sensitivity with n-type sensing material is determined by  $S = R_a/R_g$ . Conversely, for p-type material, the sensitivity is calculated according to the formula  $S = R_g/R_a$ . Here,  $R_a$  and  $R_g$  represent the resistance measured when exposed to air and reducing gases. Response–recovery time refers to the duration it takes for the sensor to demonstrate a resistance alteration of approximately 90% of the overall change following dynamic adsorption and desorption processes.

## 3 Result and discussion

### 3.1 Materials morphology

The crystalline characteristics were characterized determined *via* X-ray powder diffraction (XRD, Rigaku). According to Fig. 2, the XRD patterns clearly indicated that all samples belonged to inverse spinel structure of  $\text{NiFe}_2\text{O}_4$ , which perfectly matched the reference PDF#74-2081. The characteristic peaks observed at  $2\theta = 18.415^\circ$ ,  $30.290^\circ$ ,  $35.685^\circ$ ,  $53.819^\circ$  and  $57.375^\circ$  were assigned to the crystallographic planes (111), (220), (311), (422) and (511) of  $\text{NiFe}_2\text{O}_4$ , respectively. In addition, for samples with lower Ni element content (Ni/Fe-1 and Ni/Fe-2), the diffraction peaks of  $\text{Fe}_2\text{O}_3$  at  $2\theta$  of  $24.128^\circ$  and  $33.117^\circ$  were identified as (012) and (104) planes, respectively (PDF#72-0469). As the increase of Ni element content, the diffraction peaks belonging to  $\text{Fe}_2\text{O}_3$  gradually disappeared, and diffraction peaks attributed to NiO appeared in the XRD patterns. The peaks observed at  $37.334^\circ$ ,  $43.380^\circ$  and  $63.023^\circ$  were identified as belonging to the NiO phase. These peaks were defined as the (111), (200) and (220) crystallographic planes of NiO according to PDF#73-1519. Sharp diffraction peaks indicates that the materials are well crystallized. No other peaks were found besides the diffraction peaks

corresponding to  $\text{NiFe}_2\text{O}_4$ ,  $\text{Fe}_2\text{O}_3$  and NiO, implying the absence of other compounds in the samples.

The nanomaterial's average diameters were determined using Scherrer's formula ( $D = 0.89\lambda/\beta \cos \theta$ ).<sup>11</sup> The approximate values for Ni/Fe-1, Ni/Fe-2, Ni/Fe-4, Ni/Fe-6, Ni/Fe-8 and Ni/Fe-10 samples were calculated at approximately 37.7 nm, 30.0 nm, 9.6 nm, 10.3 nm, 9.7 nm and 11.0 nm, respectively. For samples with lower Ni element content, their average crystal sizes were relatively large, around 30 nm or above. For samples with a Ni/Fe atomic ratio greater than 20%, the crystal size decreased to around 10 nm. The observed variation in crystal size can be attributed to the differences in grain size between  $\text{Fe}_2\text{O}_3$  and NiO. The larger grain size of  $\text{Fe}_2\text{O}_3$  compared to NiO may have contributed to the larger crystal sizes observed in samples with lesser Ni content. With increasing Ni content, the samples gradually transitioned from being predominantly  $\text{Fe}_2\text{O}_3$ -loaded to being NiO-loaded. So that, the transition in composition likely influenced the grain size of the material, resulting in the observed trend.

The surface morphology and grain size characteristics were explored *via* scanning electron microscopy (SEM, Gemini SEM 300) analysis of the obtained materials. Representative SEM images observed that the prepared nanomaterials appeared as cubic nanoblocks, with a particle size of approximately 20  $\mu\text{m}$  (as displayed in Fig. 3). For samples with lower Ni element content, two different sizes of nanospheres, 125 nm and 20 nm, can be distinctly discerned on the exterior of the prepared nanoblocks. Due to the nanoblocks being assembled from differently sized nanospheres, the nanomaterials exhibit a rich porosity, giving rise to a rough surface on the nanoblocks. However, for other samples with higher Ni element content, the nanoblocks were stacked by uniform nanospheres at approximately 10 nm. No larger nanospheres were observed. The uniform size of the nanospheres results in relatively small pores between them, thereby forming relatively dense and smooth nanoblocks. As seen by the sizes distribution map, the Ni/Fe-1, Ni/Fe-2, Ni/Fe-4, Ni/Fe-6, Ni/Fe-8 and Ni/Fe-10 samples were determined to have approximate average dimensions of 38.74 nm, 27.99 nm, 11.95 nm, 12.67 nm, 12.82 nm, 12.73 nm, respectively. The SEM characterization results are consistent with the XRD analysis results. For samples with lower Ni element content, the nanomaterials have larger crystal sizes, while as the Ni element content increases, the crystal size of the nanomaterials decreases. As we all know, higher porosity in sensing materials may facilitate gases diffusion. In accordance with the morphological characteristics of the material, it can be reasonably deduced that samples with lower Ni content possess better gas-sensing properties.

### 3.2 Gas sensing performances

Gas sensor's responses to 10 ppm *n*-butanol were gauged in the temperature interval of 100 to 160  $^\circ\text{C}$  to ascertain the optimum operating temperature. All sensors exhibit a "volcano-shaped" trend<sup>12</sup> as presented in Fig. 4(a). With the rising temperature, the responses initially increase and subsequently decrease. At low temperatures, gas sensors typically exhibit low sensitivity

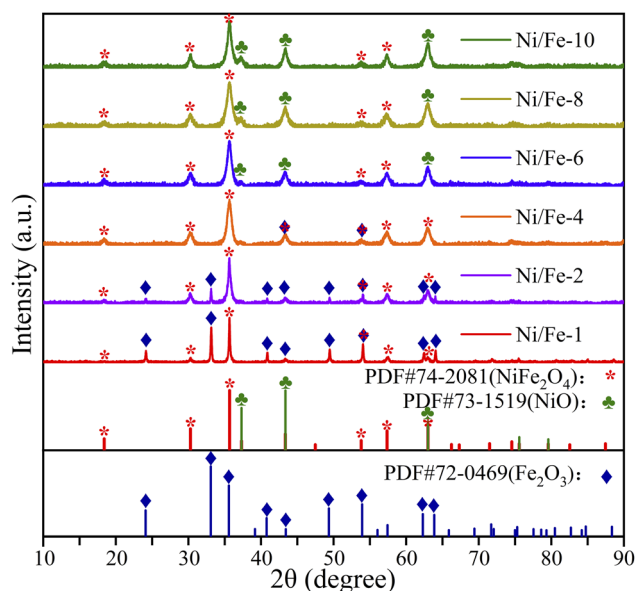


Fig. 2 XRD patterns of all materials.





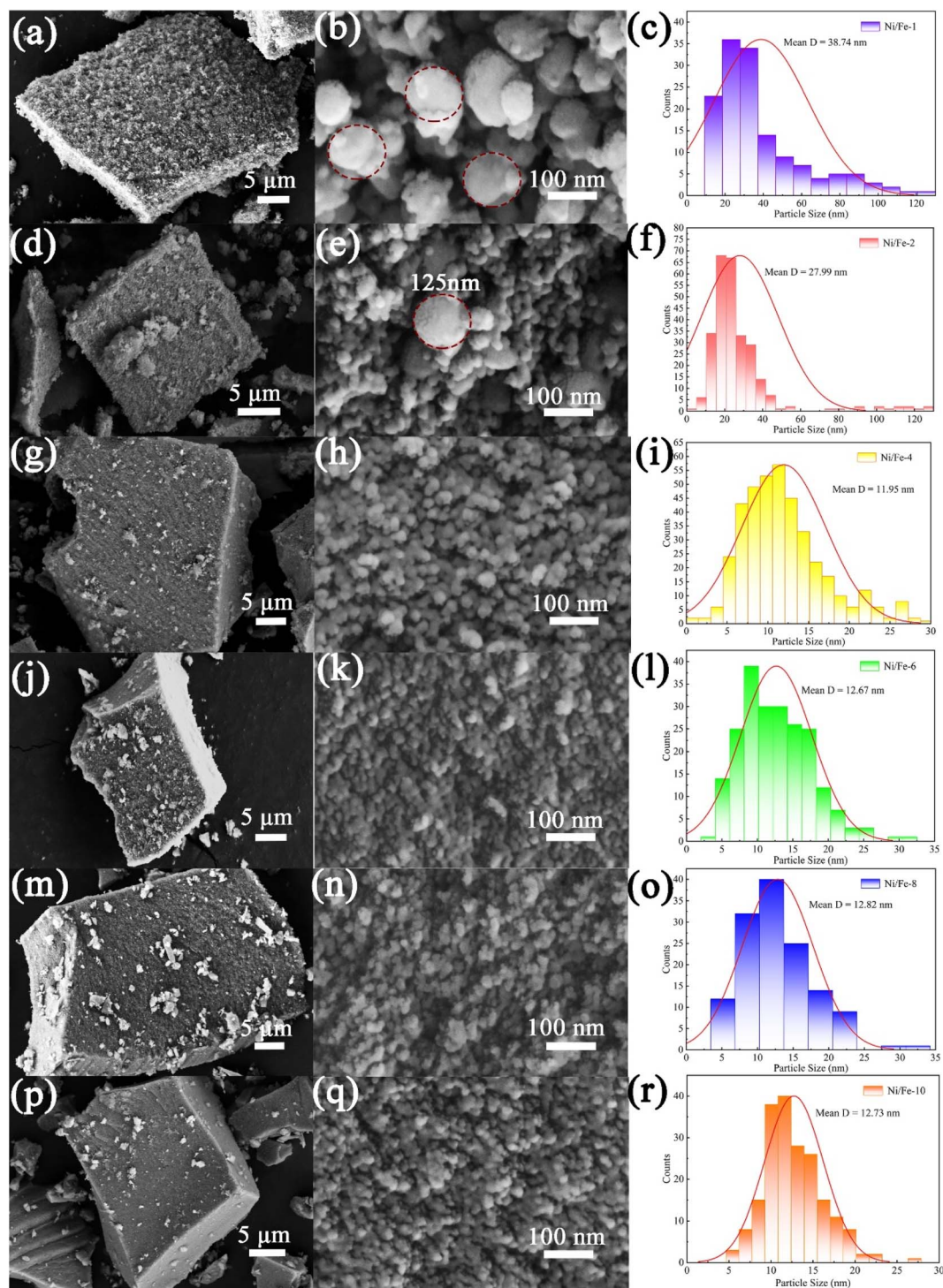


Fig. 3 The SEM images and particle sizes distribution maps of the (a–c) Ni/Fe-1, (d–f) Ni/Fe-2, (g–i) Ni/Fe-4, (j–l) Ni/Fe-6, (m–o) Ni/Fe-8, (p–r) Ni/Fe-10.

since gas molecules do not possess sufficient energy to bind chemisorbed oxygen ions. As the operating temperature further rises, the sensitivity increases owing to enhanced reaction kinetics and increased gas diffusion. However, when the operating temperature exceeds a certain threshold, gas molecules do not fully react with the chemisorbed oxygen ions before

escaping from the material.<sup>13</sup> Consequently, excessively high temperatures can decrease the sensitivity of gas sensors. According to the data presented in Fig. 4(a), all gas sensors attain the maximum response at 130 °C. In addition to that, the Ni/Fe-2 gas sensor demonstrates the highest response (29.747), which is approximately three to sixfold greater than that of

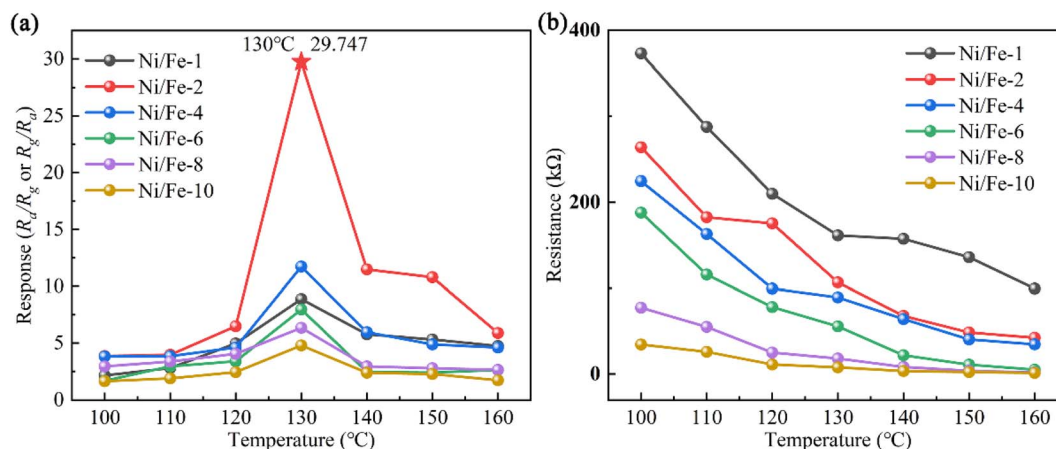


Fig. 4 (a) The responses of sensors in the range of 100–160 °C. (b) Variation of sensor resistances ( $R_a$ ) at various temperatures.

others. The increased gas sensitivity is mainly attributed to the Ni/Fe-2 composite composed of nanoblocks assembled from different sized nanospheres. The distinctive structure gives rise to a high porosity surface, which promotes gas adsorption and desorption. In conclusion, the Ni/Fe-2 sensor exhibits superior gas sensitivity towards *n*-butanol.

The resistance variation of sensors with the operating temperature at 100–160 °C is depicted in Fig. 4(b). The results apparently indicate that with the ascending operating temperature, the sensor resistances noticeably decrease. The observed phenomenon aligns with the electrical characteristics of semiconductor materials.<sup>14</sup> When the sensor is exposed to air, oxygen captures electrons within the nanomaterial and then adsorbs onto the surface as oxygen ions. Consequently, for *n*-type sensing materials, the decrease in carrier concentration increases material resistance. Conversely, for *p*-type sensing materials, oxygen adsorption raises hole concentration, reducing the material's resistance. Therefore, a deduction can be made that the resistance of the *n*-type sensor exceeds that of the *p*-type sensor. Furthermore, over the entire temperature range, the samples with low Ni element content exhibited higher resistances than those with higher content, which arises from the synergistic interplay between the material's oxygen adsorption capacity and electron mobility.<sup>10</sup> These findings emphasize the potential for further enhancement of gas sensitivity in Ni/Fe-2 sensor.

As indicated in Fig. 5, the response–recovery characteristics of all gas sensors were examined. Among them, Ni/Fe-2 gas sensor displays the shortest response time of 16 s. Fe<sub>2</sub>O<sub>3</sub> is an *n*-type sensing material, while NiO is classified as a *p*-type sensing material.<sup>15</sup> When the Ni content in the composite material is low, the presence of Fe<sub>2</sub>O<sub>3</sub> causes the sensors to exhibit *n*-type sensing behavior. However, once the Ni/Fe atomic ratio surpasses 40%, the gradual increase in NiO content causes the sensors exhibit *p*-type sensing characteristics. In semiconductors, *n*-type semiconductors have a higher electron concentration, and electron mobility is typically higher than hole mobility.<sup>16,17</sup> Such characteristics facilitate the faster transmission of electrons to the sensor surface. Consequently,

*n*-type sensors tend to demonstrate shorter response times than *p*-type sensors. The SEM characterization images reveal that the Ni/Fe-2 nanoblocks surface exhibits abundant pores, which increase the channels for gas ingress and egress. Therefore, the response speed of the Ni/Fe-2 sensor is faster than that of other sensors. The longer recovery time of the *n*-type sensor when compared to the *p*-type sensor can be attributed to the effect of the barrier. At low temperatures, insufficient energy hinders the electron's ability to overcome the energy barrier, and the adsorbed *n*-butanol gas also struggles to desorb from the material surface.<sup>14,18</sup> As a result, this leads to longer recovery times for the sensor. In summary, the Ni/Fe-2 sensor manifests superior response–recovery properties compared to others and is thus deemed the optimum device.

The sensors' dynamic sensing characteristics across varying concentrations of *n*-butanol at 130 °C, as revealed in Fig. 6. The nested figures within Fig. 6 clearly demonstrate that the sensors displayed favourable linear correlation, with linear fitting coefficients ( $R^2$ ) exceeding 0.95 for all sensors. In particular, Ni/Fe-2 sensor manifests linear fit function of  $Y = 2.71 \times x + 2.74$ , with  $R^2$  of 0.999. The almost linear relationship indicates that the gas concentration of *n*-butanol in the environment can be estimated by inverse application of the sensor response values, with significant implications for environmental monitoring and air quality evaluation.

As evident in Fig. 7, the increase rate of sensor responses substantially diminishes when the gas concentration exceeds 10 ppm, which arises from the saturation of adsorption sites provided by the materials. The illustration apparently indicates the sensor responses are 2.569, 2.948, 2.676, 2.184, 2.081 and 1.981 even at a low *n*-butanol gas concentration of 250 ppb. Low detection limit demonstrates that the Ni/Fe-2 sensor is well-suited to detect *n*-butanol at trace levels.

The repeatability of the Ni/Fe-2 gas sensor upon six reversible cycles of sensitivity tests to 10 ppm of *n*-butanol at 130 °C is presented in Fig. 8. The Ni/Fe-2 sensor exhibited consistent response and recovery characteristics during each reversible cycle, while the response values demonstrated approximately 29.7. The Ni/Fe-2 gas sensor consistently exhibits



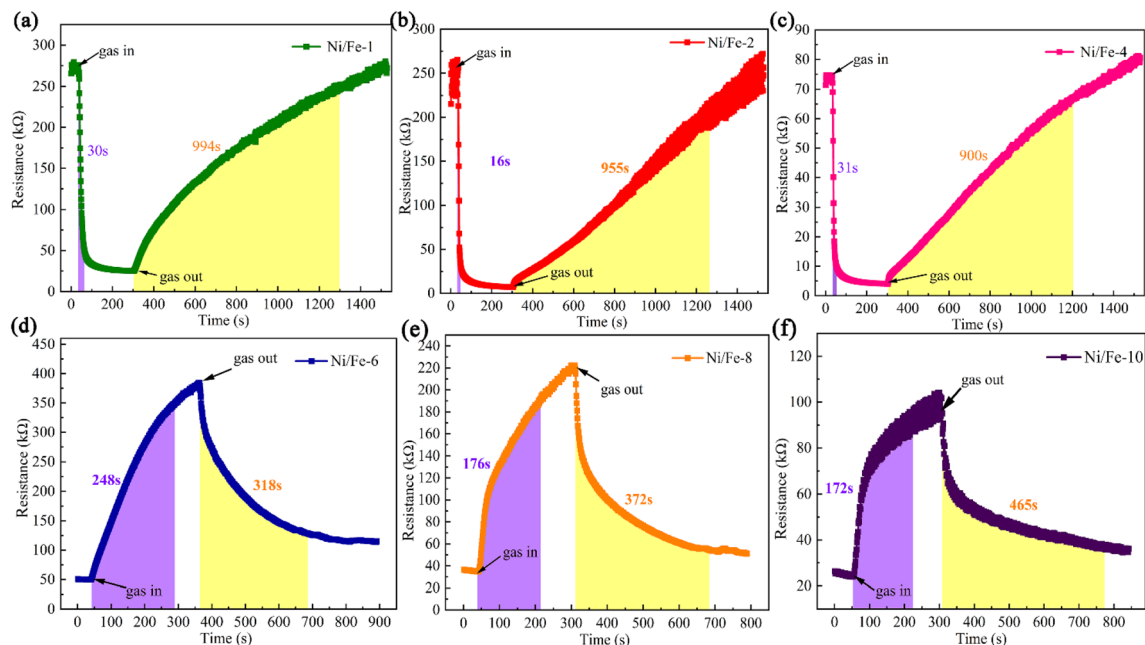


Fig. 5 The six sensors' response–recovery properties (130 °C, 10 ppm *n*-butanol).

a commendable level of repeatability within an acceptable range of deviation.

As illustrated in Fig. 9, 10 ppm various gases including *n*-butanol, acetone, triethylamine, xylene, ethanol, trimethylamine, methanol, formaldehyde, and ammonia have been chosen to evaluate the selectivity of the six sensors with different Ni/Fe atomic ratios at optimal operating temperature. The discriminative capability of the gas sensors can be ascribed to the impact of the alkyl chain length on the various gas

molecules.<sup>19</sup> As the length of the alkyl chain increases, so does the carrier concentration, resulting in a higher sensor response value.<sup>20–22</sup> Evidently, the Ni/Fe-2 sensor exhibited significantly lower responses to both ammonia and methanol, while exhibiting notably higher responses to *n*-butanol gas. The observation indicates that the Ni/Fe-2 sensor has excellent selectivity and the potential to effectively differentiate multiple gases. Furthermore, sensor's responses to all target gases generally exhibits an initial increase followed by a decrease as the content

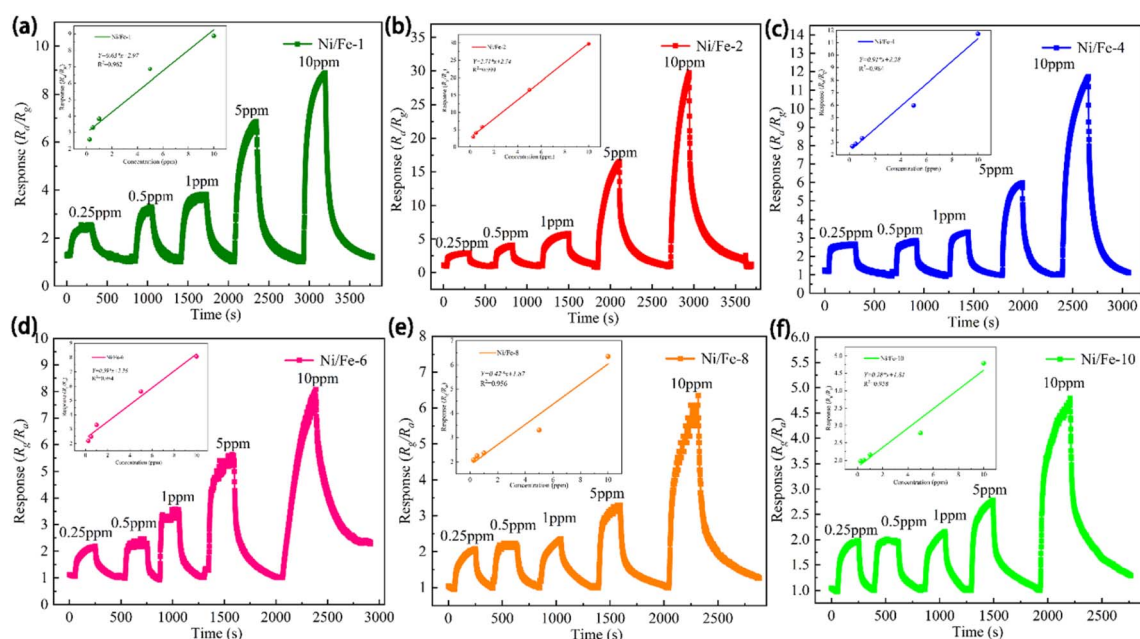


Fig. 6 The dynamic resistance versus time.





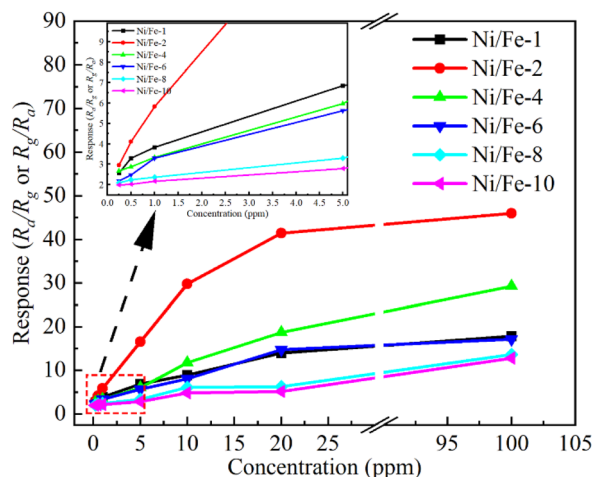


Fig. 7 Sensitivity values vary with concentration at 130 °C.

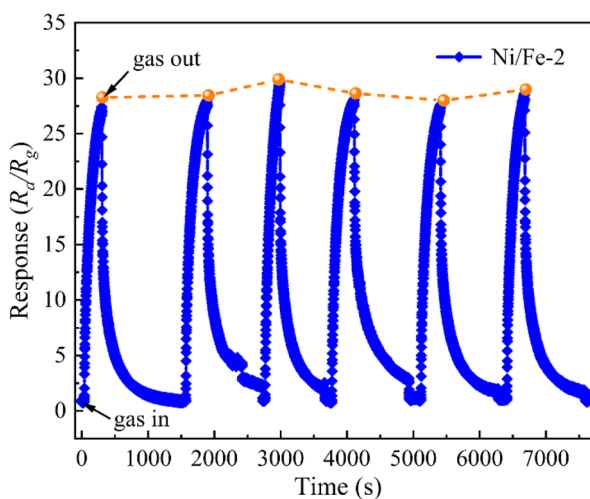


Fig. 8 The repeatability to 10 ppm *n*-butanol for Ni/Fe-2 sensor at 130 °C.

of Ni content increased, further proving that the optimal doping ratio for Ni/Fe-based sensors is Ni/Fe = 2 : 10.

Table 1 compares the gas sensitivity characteristics among several *n*-butanol gas sensors. The result indicates a consistent observation that gas sensors functioning at lower operating temperatures generally demonstrate diminished response values. Conversely, sensors exhibiting higher response values tend to operate within the temperature range of approximately 300–400 °C. In comparison, the Ni/Fe-2 gas sensor prepared in this paper demonstrates the lowest operating temperature among the sensors listed in Table 1, reaching only 130 °C. In addition, the Ni/Fe-2 sensor also demonstrates a fast response characteristic, which can be ascribed to the notable augmentation in pore quantity, thereby increasing the transmission channel of gas molecules. Nevertheless, the Ni/Fe-2 sensor also exhibits a longer recovery time, which may be attributed to the insufficient energy for gas molecules to desorb from

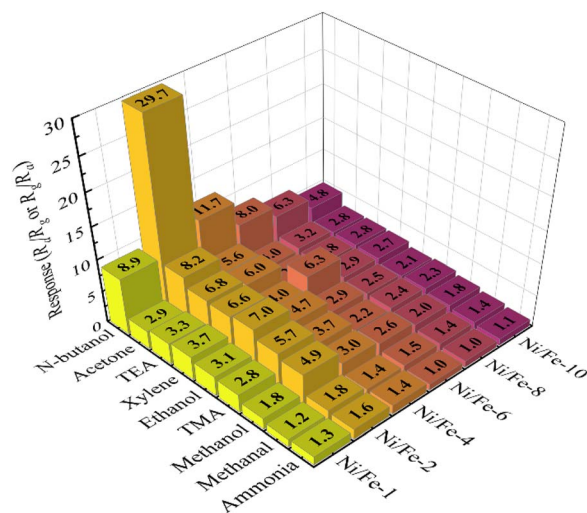


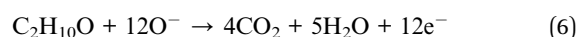
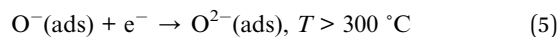
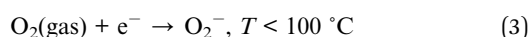
Fig. 9 Selectivity of Ni/Fe-2 sensor to various gases at 130 °C.

nanomaterials. Overall, Ni/Fe-2 sensor demonstrates exceptional potential and is suitable for the identification of *n*-butanol.

### 3.3 Gas sensing mechanism

Given the analysis that came before, it can be reasonably inferred that the Ni/Fe-2 nanocomposite is primarily composed of Fe<sub>2</sub>O<sub>3</sub> and NiFe<sub>2</sub>O<sub>4</sub>, which exhibit n-type sensing characteristics. Oxygen molecules absorb electrons in the conduction band<sup>23</sup> when the Ni/Fe-2 nanocomposite contact ambient air. Depending on the environmental temperature, adsorbed oxygen ions (O<sub>2</sub><sup>-</sup>, O<sup>-</sup>, O<sup>2-</sup>) are generated. The decreased carrier concentration and the electron depletion layer cause increased resistance.

The reaction processes are apparent in eqn (2)–(5).<sup>24</sup>



When the Ni/Fe-2 sensor is placed in an atmosphere of *n*-butanol, the gas molecules undergo an oxidation–reduction reaction with the adsorbed oxygen ions (O<sup>-</sup>) (eqn (6)).<sup>35</sup> The electrons that were captured previously are freed into the Ni/Fe-2 nanocomposite conduction band and recombine with the electron vacancies situated in the valence band (eqn (7)).<sup>36</sup> The electron depletion layer's thickness on the Ni/Fe-2 nanocomposite has reduced, causing a decrease in the Ni/Fe-2 sensor resistance when exposed to *n*-butanol. The potential gas



Table 1 Gas sensitivity characteristics among different *n*-butanol gas sensors

Materials	<i>T</i> (°C)	Conc. (ppm)	Response ( $R_a/R_g$ or $R_g/R_a$ )	$t_{res}/t_{rec}$	Ref.
NiO nanoprisms/Fe <sub>2</sub> O <sub>3</sub> nanosheets	200	100	24.15	120 s/64 s	6
Ni-Co <sub>3</sub> O <sub>4</sub> nanoflower	165	100	8.34	59 s/63 s	11
3D Sb-doped ZnFe <sub>2</sub> O <sub>4</sub> spheres	250	100	35.5	4 s/250 s	18
Tourmaline@ZnO	320	100	120.84	—/—	19
Fe <sub>2</sub> O <sub>3</sub> /rGO nanocube	RT	100	2.71	53 s/42 s	25
Au-Pd decorated hierarchical WO <sub>3</sub> nanowire bundles	200	100	93	4 s/12 s	26
α-Fe <sub>2</sub> O <sub>3</sub> /ZnFe <sub>2</sub> O <sub>4</sub>	160	1	3.25	15 s/4 s	27
ZnO-NiO	400	100	186	3 s/208 s	28
Au-LaFeO <sub>3</sub> core-shell	225	100	115	38 s/19 s	29
Co <sub>3</sub> O <sub>4</sub> -CuO-CuOHF	180	100	120	160 s/250 s	30
Co-BiVO <sub>4</sub>	300	100	51.8	149 s/38 s	31
Al-CdIn <sub>2</sub> O <sub>4</sub> nanofiber	300	200	68.68	16 s/17 s	32
1.5% In <sub>2</sub> O <sub>3</sub> -SnO <sub>2</sub>	140	10	5.96	—/—	33
ZnO-In <sub>2</sub> O <sub>3</sub>	180	50	99.5	—/—	34
Ni/Fe-2	130	0.25	2.948	30 s/115 s	This paper
		10	29.747	16 s/955 s	

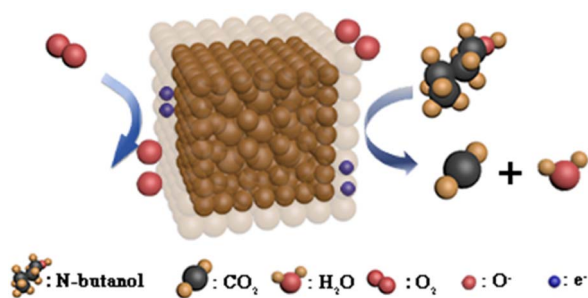


Fig. 10 The potential gas detection mechanism for Ni/Fe-2 sensor.

detection mechanism for the Ni/Fe-2 sensor is illustrated in Fig. 10.

X-ray photoelectron spectroscopy (XPS, Thermo Scientific ESCALAB Xi+) was utilized for the characterization analysis to obtain additional insights into the chemistry valence and binding energy of the Ni/Fe-2 nanocomposite. The transition energies of various elements were calibrated utilizing the C 1s (284.8 eV) and the factors that enhance gas-sensing performance were further investigated. As illustrated in Fig. 11(a), only distinct peaks corresponding to Fe, Ni, and O elements are present in the XPS full scan spectrum, suggesting the absence of any additional impurities in the Ni/Fe-2 nanomaterial. Fig. 11(b) illustrates the Fe 2p fine scan spectrum of Ni/Fe-2. The Fe 2p<sub>1/2</sub> (724.4 eV) is deconvoluted into two distinct peaks with binding energies corresponding to 725.1 ± 0.3 eV and 723.4 ± 0.1 eV, respectively. And the Fe 2p<sub>3/2</sub> (710.7 eV) is deconvoluted into two individual peaks, characterized by binding energies of 712.3 ± 0.3 eV and 710.3 ± 0.2 eV,<sup>37</sup> respectively. Among them, the peaks at 725.1 ± 0.3 eV and 712.3 ± 0.3 eV correspond to Fe<sup>3+</sup>, while the peaks at 723.4 ± 0.1 eV and 710.3 ± 0.2 eV are classified as Fe<sup>2+</sup> state.<sup>14</sup> The existence of Fe<sup>2+</sup> indicates that the Ni/Fe-2 composite possesses more redox-active sites, which is favorable for

surface reactions to occur. The fine scan spectrum of Ni 2p region for Ni/Fe-2 was illustrated in Fig. 11(c). Specifically, the primary peak of Ni 2p<sub>1/2</sub> was identified at approximately 872.3 ± 1.7 eV, accompanied by a satellite peak at 879.7 ± 1.3 eV. While the primary peak of Ni 2p<sub>3/2</sub> was detected at approximately 854.9 ± 0.1 eV, alongside a satellite peak at 861.8 ± 1.2 eV. Moreover, Ni<sup>3+</sup> and Ni<sup>2+</sup> peaks in Ni 2p<sub>1/2</sub> were respectively placed at 873.8 ± 1.1 eV and 872.3 ± 0.1 eV. Similarly, Ni<sup>3+</sup> and Ni<sup>2+</sup> peaks in Ni 2p<sub>3/2</sub> were located at 855.5 ± 1.7 eV and 854.8 ± 0.1 eV, respectively.<sup>38</sup> According to the XPS characterization analysis, the Ni<sup>3+</sup> content in Ni/Fe-2 is significantly higher than that of Ni<sup>2+</sup>. The higher concentration of Ni<sup>3+</sup> ions would correlate with elevated levels of oxygen content.<sup>12</sup> From the fine scan spectrum of O 1s (Fig. 11(d)), the three evident peaks at 529.9 ± 0.2 eV, 531.7 ± 0.2 eV and 533.4 ± 0.1 eV are corresponding to crystal lattice oxygen (O<sub>L</sub>), oxygen vacancies (O<sub>V</sub>) and chemisorbed oxygen (O<sub>C</sub>), respectively.<sup>39</sup> The table presented in Fig. 11(d) displays the relative area percentages of different oxygen species. As widely acknowledged, the gas sensing characteristics are intricately linked to the O<sub>V</sub> content that exists at the nanomaterial's surface. The occurrence of O<sub>V</sub> may amplify the count of redox-active sites, hence facilitate redox reactions.<sup>40</sup> A higher quantity of adsorption sites correlates with improved sensor performance.

The transmission electron microscopy (TEM, JEM 2100 F) analysis in Fig. 12(a) and (b) displayed that two distinct sizes of nanospheres can be readily discerned on the surface of the Ni/Fe-2 nanoblocks, measuring approximately 125 nm and 20 nm, respectively. This finding aligns with the SEM images illustrated in Fig. 3(d) and (e). Lattice fringes corresponding to the crystal structures of Fe<sub>2</sub>O<sub>3</sub> and NiFe<sub>2</sub>O<sub>4</sub> are revealed in the high-resolution electron microscopy (HRTEM, JEM 2100 F) images of Ni/Fe-2 material (Fig. 12(c) and (d)), while no lattice fringes related to NiO are observed. The HRTEM analysis further suggests that the composition of Ni/Fe-2 comprises Fe<sub>2</sub>O<sub>3</sub> and NiFe<sub>2</sub>O<sub>4</sub>, with no NiO in this sample. The selective area electron





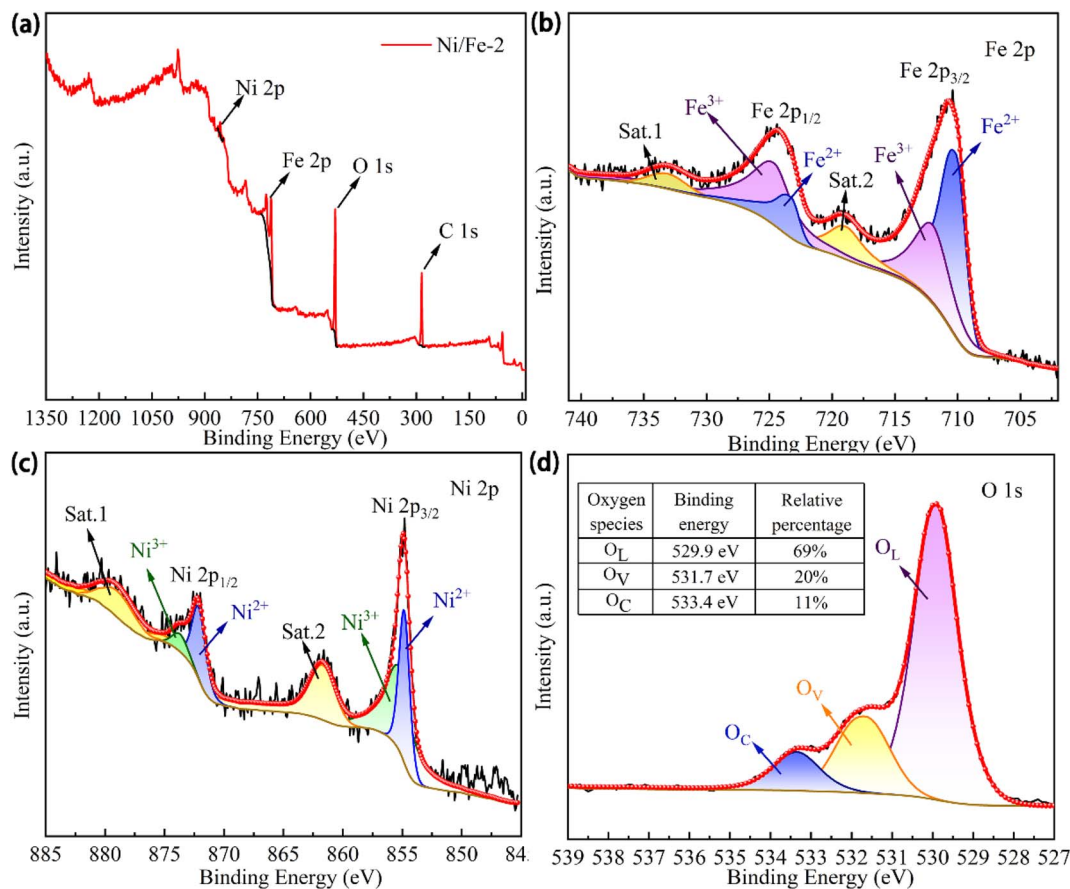


Fig. 11 XPS spectra of Ni/Fe-2 nanoblocks.

diffraction (SAED, JEM 2100 F) pattern of Ni/Fe-2 shown in Fig. 12(e) displays clear diffraction rings, indicating that the composite material has a well-crystallized polycrystalline structure.

In summary, the Ni/Fe-2 sensor's enhanced gas-sensing abilities are caused by the following factors:

First and foremost, gas-sensing performance is significantly influenced by the morphological characteristics of materials.

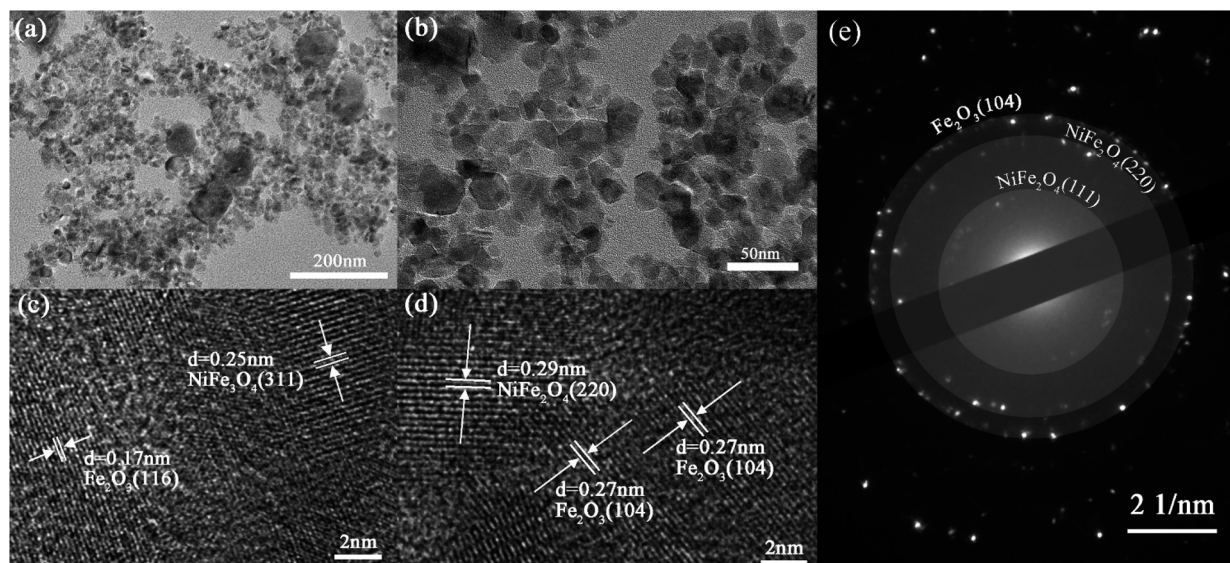


Fig. 12 (a, b) TEM, (c, d) HRTEM and (e) SAED pattern of the Ni/Fe-2 nanoblocks.



Based on the SEM images, samples with low Ni content display a rough surface, while the nanospheres become more uniform in size on the surface of the nanoblocks as Ni content increases, resulting in an increase in surface flatness. From the SEM and TEM characterization images, Ni/Fe-2 nanocomposite exhibits nanoblocks formed by the aggregation of distinct sizes of nanospheres. The presence of nanospheres with varying sizes enhances the porosity of Ni/Fe-2 nanocomposite, leading to a roughened surface. The rough surface can enhance the number of redox active sites on the surface, leading to greater adsorption of gas molecules on the material. This significantly improves the gas-sensitive attributes of the material.<sup>41</sup> The aforementioned characteristics create additional transmission channels for gas molecules to be adsorbed, thereby enabling the Ni/Fe-2 sensor to exhibit faster response times. However, gas molecules adsorbed within the material have difficulty desorbing from the material due to the low operating temperature. This is highly likely to be a significant contributing factor to the extended response time.

Additionally, the formation of heterojunctions can significantly improve sensing performance. The band diagrams of  $\text{Fe}_2\text{O}_3$  and  $\text{NiFe}_2\text{O}_4$  before contact are depicted in Fig. 13(a). P-n heterojunctions are established on the contact interfaces<sup>42</sup> owing to the difference in work functions between n-type  $\text{Fe}_2\text{O}_3$  (5.9 eV)<sup>25</sup> and p-type  $\text{NiFe}_2\text{O}_4$  (4.61 eV).<sup>9,43</sup> During this process, electrons within the  $\text{NiFe}_2\text{O}_4$  conduction band ( $E_C$ ) migrate towards the  $\text{Fe}_2\text{O}_3$   $E_C$  until their Fermi level reaches equilibrium (Fig. 13). As depicted in Fig. 13(b), the electron depletion layer (EDL) and hole depletion layer (HDL) are located at the interface, which causes a reduction in carrier concentration and the formation of a high-resistance interface state in the sensor. Furthermore, the existence of a barrier restricts the free conduction of electrons. Electrons lack sufficient energy to overcome the barrier at lower temperatures, which is a contributing factor to the sensor's extended recovery time.

Finally, the content of oxygen vacancies at the nanomaterial is also a crucial factor influencing its gas sensing. The  $\text{Ni}^{3+}/\text{Ni}^{2+}$  and  $\text{Fe}^{3+}/\text{Fe}^{2+}$  ions existed in  $\text{NiFe}_2\text{O}_4$ , which increased the redox-active sites on nanomaterial surfaces, hence promoting the gas reaction. The presence of  $\text{Fe}^{2+}$  contributes to a higher number of redox-active sites, while  $\text{Ni}^{3+}$  further enhances the chemical oxygen content in the nanomaterial. Therefore, Ni/Fe-2 materials exhibit superior capacity to absorb oxygen, leading to an improvement in the oxidation reaction.<sup>44</sup> With the catalytic action of the  $\text{Ni}^{3+}$  ions, the Ni/Fe-2 material exhibits improved gas sensing capabilities towards *n*-butanol gas.

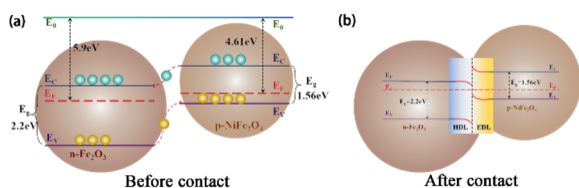


Fig. 13 Bandgap diagram for Ni/Fe-2 nanoblocks.

## 4 Conclusions

In conclusion, the  $\text{NiFe}_2\text{O}_4$ -based nanoblocks were synthesized using hydrothermal method with varying Ni/Fe atomic ratios. The Ni/Fe-2 gas sensor exhibited excellent gas sensing performance (29.747) towards 10 ppm *n*-butanol at 130 °C. Compared to most *n*-butanol sensors, the Ni/Fe-2 sensor prepared in this paper demonstrated lower operating temperature, quick response (16 s) and extremely low detection limit. The improved gas sensing performance of the Ni/Fe-2 sensor can be attributed to the unique structure of the nanocubes, which increases the material's specific surface area. Additionally, the formation of heterojunctions and the increase in oxygen vacancy content also promote redox reactions. Therefore, the Ni/Fe-2 sensor has provided a highly feasible approach for achieving ppb-level trace detection of *n*-butanol.

## Conflicts of interest

There are no conflicts to declare.

## Acknowledgements

Project supported by the Shandong Natural Science Foundation (ZR2019BF030) and the Development Plan of Youth Innovation Team of University in Shandong Province (Grant No. 2022KJJ005).

## Notes and references

- 1 B. Yao, X. Cui, X. Tian, X. Xing, T. Chen and Y. Wang,  $\text{SnO}_2$  submicron porous cube derived from metal-organic framework for *n*-butanol sensing at room temperature, *Ceram. Int.*, 2023, **49**, 25477–25485.
- 2 O. M. Perrone, A. C. Roveda, D. A. de Moraes and D. P. Volanti, The enhanced *n*-butanol sensing performance of  $\text{In}_2\text{O}_3$  loaded NiO cuboid heterostructure, *J. Alloys Compd.*, 2023, **930**, 167483–167490.
- 3 Q. Zhang, Q. Ma, X. Wang, Y. Wang and D. Zhao, Surface double oxygen defect engineering in button-shaped porous  $\text{CeO}_2/\text{WO}_{2.9}$  heterostructures for excellent *n*-butanol detection at room temperature, *Appl. Surf. Sci.*, 2023, **616**, 156536–156545.
- 4 Y. Li, L.-X. Shan, R.-C. Wang, X.-X. Lian and Q.-J. Zhou, Enhanced *n*-butanol sensing performance of  $\text{SnO}_2/\text{ZnO}$  nanoflowers fabricated via a facile solvothermal method, *Ceram. Int.*, 2022, **48**, 22426–22434.
- 5 C. Dai, M. Chen, Y. Lin, R. Qi, C. Luo, H. Peng and H. Lin, High performance gas sensors based on layered cobaltite nanoflakes with moisture resistance, *Appl. Surf. Sci.*, 2022, **604**, 154487–154496.
- 6 H. Pan, Z. Li, C. Lou, G. Lei, J. Xie, W. Zheng, X. Liu and J. Zhang, Anchoring  $\text{Fe}_2\text{O}_3$  nanosheets on NiO nanoprisms to regulate the electronic properties for improved *n*-butanol detection, *Sens. Actuators, B*, 2022, **354**, 131223–131232.



- 7 Y. Zhang, C. Jia, Q. Wang, Q. Kong, G. Chen, H. Guan and C. Dong, Highly sensitive and selective toluene sensor of bimetallic Ni/Fe-MOFs derived porous  $\text{NiFe}_2\text{O}_4$  nanorods, *Ind. Eng. Chem. Res.*, 2019, **58**, 9450–9457.
- 8 N. Liu, X.-F. Wang, G. Zhang, H. Liang, T. Li, Y. Zhao, T. Zhang, Z. Tan and X.-Z. Song, Metal–organic framework-derived porous  $\text{NiFe}_2\text{O}_4$  nanoboxes for ethyl acetate gas sensors, *ACS Appl. Nano Mater.*, 2022, **5**, 14320–14327.
- 9 J. Yang, B. Jiang, X. Wang, C. Wang, Y. Sun, H. Zhang, K. Shimano and G. Lu, MOF-derived porous NiO/ $\text{NiFe}_2\text{O}_4$  nanocubes for improving the acetone detection, *Sens. Actuators, B*, 2022, **366**, 131985–131995.
- 10 C. Wang, Y. Wang, P. Cheng, L. Xu, F. Dang, T. Wang and Z. Lei, In-situ generated  $\text{TiO}_2/\alpha\text{-Fe}_2\text{O}_3$  heterojunction arrays for batch manufacturing of conductometric acetone gas sensors, *Sens. Actuators, B*, 2021, **340**, 129926–129936.
- 11 P. Cheng, F. Dang, Y. Wang, J. Gao, L. Xu, C. Wang, L. Lv, X. Li, B. Zhang and B. Liu, Gas sensor towards n-butanol at low temperature detection: Hierarchical flower-like Ni-doped  $\text{Co}_3\text{O}_4$  based on solvent-dependent synthesis, *Sens. Actuators, B*, 2021, **328**, 129028–129039.
- 12 J. Yang, W. Han, J. Ma, C. Wang, K. Shimano, S. Zhang, Y. Sun, P. Cheng, Y. Wang, H. Zhang and G. Lu, Sn doping effect on NiO hollow nanofibers based gas sensors about the humidity dependence for triethylamine detection, *Sens. Actuators, B*, 2021, **340**, 129971–129983.
- 13 U. T. Nakate, R. Ahmad, P. Patil, Y. T. Yu and Y.-B. Hahn, Ultra thin NiO nanosheets for high performance hydrogen gas sensor device, *Appl. Surf. Sci.*, 2020, **506**, 144971–144978.
- 14 Z. Lei, P. Cheng, Y. Wang, L. Xu, L. Lv, X. Li, S. Sun, X. Hao, Y. Zhang, Y. Zhang and Z. Weng, Pt-doped  $\alpha\text{-Fe}_2\text{O}_3$  mesoporous microspheres with low-temperature ultra-sensitive properties for gas sensors in diabetes detection, *Appl. Surf. Sci.*, 2023, **607**, 154558–154570.
- 15 N. Jayababu, M. Poloju, J. Shruthi and M. V. R. Reddy, NiO decorated  $\text{CeO}_2$  nanostructures as room temperature isopropanol gas sensors, *RSC Adv.*, 2019, **9**, 13765–13775.
- 16 R. G. Kepler, P. M. Beeson, S. J. Jacobs, R. A. Anderson, M. B. Sinclair, V. S. Valencia and P. A. Cahill, Electron and hole mobility in tris(8hydroxyquinolinolatoN<sub>1</sub>O<sub>8</sub>) aluminum, *Appl. Phys. Lett.*, 1995, **66**(26), 3618–3620.
- 17 Y. Takeda, A. Sasaki, Y. Imamura and T. Takagi, Electron mobility and energy gap of  $\text{In}_{0.53}\text{Ga}_{0.47}\text{As}$  on InP substrate, *J. Appl. Phys.*, 2008, **47**, 5405–5408.
- 18 L. Lv, P. Cheng, Y. Wang, L. Xu, B. Zhang, C. Lv, J. Ma and Y. Zhang, Sb-doped three-dimensional  $\text{ZnFe}_2\text{O}_4$  macroporous spheres for N-butanol chemiresistive gas sensors, *Sens. Actuators, B*, 2020, **320**, 128384–128394.
- 19 L. Sun, Y. Guo, Y. Hu, S. Pan and Z. Jiao, Conductometric n-butanol gas sensor based on Tourmaline@ZnO hierarchical micro-nanostructures, *Sens. Actuators, B*, 2021, **337**, 129793–129803.
- 20 X. Liu, J. Zhang, X. Guo, S. Wu and S. Wang, Enhanced sensor response of Ni-doped  $\text{SnO}_2$  hollow spheres, *Sens. Actuators, B*, 2011, **152**, 162–167.
- 21 N. Swaminathana, A. Henninga, T. Jurca, J. Hayona, G. Shalevc and Y. Rosenwaks, Effect of varying chain length of n-alcohols and n-alkanes detected with electrostatically-formed nanowire sensor, *Sens. Actuators, B*, 2017, **248**, 240–246.
- 22 H. Park, J.-H. Kim, D. Vivod, S. Kim, A. Mirzaei, D. Zahn, C. Park, S. S. Kim and M. Halik, Chemical-recognition-driven selectivity of  $\text{SnO}_2$ -nanowire-based gas sensors, *Nano Today*, 2021, **40**, 101265–101277.
- 23 Q. Qin, Y. Zhang, W. Bu, N. Liu, Z. Zhou, C. Hu and X. Chuai, Hierarchical porous  $\text{Fe}_2\text{O}_3$  derived from willow branch slices biotemplate with fast response and excellent selectivity for acetone, *Sens. Actuators, B*, 2023, **392**, 134079–134088.
- 24 M. K. Tiwari, S. C. Yadav, A. Srivastava, A. Kanwade, J. A. K. Satrughna, S. S. Mali, J. V. Patil, C. K. Hong and P. M. Shirage, Enhancement of CO gas sensing performance by Mn-doped porous  $\text{ZnSnO}_3$  microspheres, *RSC Adv.*, 2022, **12**, 32249–32261.
- 25 R. Mo, D. Han, C. Yang, J. Tang, F. Wang and C. Li, MOF-derived porous  $\text{Fe}_2\text{O}_3$  nanocubes combined with reduced graphene oxide for n-butanol room temperature gas sensing, *Sens. Actuators, B*, 2021, **330**, 129326–129335.
- 26 S. Zeb, X. Peng, Y. Shi, J. Su, J. Sun, M. Zhang, G. Sun, Y. Nie, Y. Cui and X. Jiang, Bimetal Au-Pd decorated hierarchical  $\text{WO}_3$  nanowire bundles for gas sensing application, *Sens. Actuators, B*, 2021, **334**, 129584–129594.
- 27 W. Yan, W. Liu, Z. Zhao, J. Wang, G. B. Nam, S. Cui, X. Shen and H. W. Jang, Humidity-independent electronic nose of  $\alpha\text{-Fe}_2\text{O}_3/\text{ZnFe}_2\text{O}_4$  heterojunctions for trace detection of N-butanol exhalation in lung cancer screening, *Sens. Actuators, B*, 2023, **384**, 133577–133586.
- 28 E. Wongrat, T. Ta-om, S. Khamprakaysit, N. Chanlek and S. Chooon, Effect of Cu or Ni addition to ZnO nanostructures on their n-butanol sensing performance, *Thin Solid Films*, 2023, **774**, 139839–139849.
- 29 J. Shao, C. Sun, H. Liu, P. He, Q. Liu, J. Sun, J. Li, G. Pan and X. Yang, Insight into Au functionalization on core-shell  $\text{LaFeO}_3$  spheres for high-response and selectivity n-butanol gas sensors with DFT study, *Sens. Actuators, B*, 2023, **382**, 133506–133515.
- 30 Z. Liao, Z. Yuan, H. Gao and F. Meng, Novel  $\text{Co}_3\text{O}_4\text{-CuO}$ -CuOHf porous sheet for high sensitivity n-butanol gas sensor at low temperature, *Sens. Actuators, B*, 2023, **384**, 133619–133629.
- 31 W. Guo, Y. Shuai, X. Liu, J. Zhang, J. Wang, K. H. Mahmoud, Z. M. El-Bahy and N. M. Mubarak, A n-butanol gas sensor with enhanced gas sensing performance based on Co-doped  $\text{BiVO}_4$  polyhedrons, *Sens. Actuators, B*, 2022, **354**, 131221–131232.
- 32 X. Tian, L. Yao, X. Cui, R. Zhao, X. Xiao and Y. Wang, Novel Al-doped  $\text{CdIn}_2\text{O}_4$  nanofibers based gas sensor for enhanced low-concentration n-butanol sensing, *Sens. Actuators, B*, 2022, **351**, 130946–130956.
- 33 D. An, N. Liu, H. Zhang, Q. Sun, C. Li, Y. Li, Q. Zhang and Y. Lu, Enhanced n-butanol sensing performance of  $\text{SnO}_2$ -based gas sensors by doping  $\text{In}_2\text{O}_3$  via co-precipitation method, *Sens. Actuators, B*, 2021, **340**, 129944–129952.





- 34 D. An, Q. Wang, X. Tong, X. Lian, Y. Zou and Y. Li, ZnO-enhanced  $\text{In}_2\text{O}_3$ -based sensors for n-butanol gas, *Ceram. Int.*, 2019, **45**, 6869–6874.
- 35 L. Li, G. Wan, X. Cui and Y. Wang, Ultrasensitive sensing performances of amphiphilic block copolymer induced gyru-like  $\text{In}_2\text{O}_3$  thick films to low-concentration acetone, *RSC Adv.*, 2023, **13**, 20575–20583.
- 36 X. Zhang, W. Du, Q. Li and C. Lv, Highly efficient ethanol vapour detection using g- $\text{C}_3\text{N}_4/\text{ZnO}$  micro flower-like heterostructural composites, *RSC Adv.*, 2022, **12**, 20618–20627.
- 37 P. Hao, G. Qiu, P. Song, Z. Yang and Q. Wang, Construction of porous  $\text{LaFeO}_3$  microspheres decorated with NiO nanosheets for high response ethanol gas sensors, *Appl. Surf. Sci.*, 2020, **515**, 146025–146032.
- 38 T. P. Mokoena, H. C. Swart, K. T. Hillie, Z. P. Tshabalala, M. Jozela, J. Tshilongo and D. E. Motaung, Enhanced propanol gas sensing performance of p-type NiO gas sensor induced by exceptionally large surface area and crystallinity, *Appl. Surf. Sci.*, 2022, **571**, 151121–151138.
- 39 T. Ai, J. Li, S. Nie, Y. Yin, J. Lu, S. Bao and L. Yan, High-performance  $\text{H}_2$  gas sensor based on Mn-doped  $\alpha\text{-Fe}_2\text{O}_3$  polyhedrons from N, N-dimethylformamide assisted hydrothermal synthesis, *Int. J. Hydrogen Energy*, 2022, **47**, 20561–20571.
- 40 W. Li, Y. Guo, Y. Liu, W. Yang, J. Hu and J. Ma, A controllable surface etching strategy for MOF-derived porous  $\text{ZnCo}_2\text{O}_4@/\text{ZnO}/\text{Co}_3\text{O}_4$  oxides and their sensing properties, *RSC Adv.*, 2023, **13**, 24936–24943.
- 41 K. Abdelkarem, R. Saad, A. M. El Sayed, M. I. Fathy, M. Shaban and H. Hamdy, Design of high-sensitivity La-doped ZnO sensors for  $\text{CO}_2$  gas detection at room temperature, *Sci. Rep.*, 2023, **13**, 18398.
- 42 Y. Xu, X. Tian, Y. Fan and Y. Sun, A formaldehyde gas sensor with improved gas response and sub-ppm level detection limit based on NiO/NiFe $_2\text{O}_4$  composite nanotetrahedrons, *Sens. Actuators, B*, 2020, **309**, 127719–127728.
- 43 K. Karupphasamy, B. Sharma, D. Vikraman, E.-B. Jo, P. Sivakumar and H.-S. Kim, Switchable p–n gas response for 3D-hierarchical NiFe $_2\text{O}_4$  porous microspheres for highly selective and sensitive toluene gas sensors, *J. Alloys Compd.*, 2021, **886**, 161281–161290.
- 44 C. Zhou, F. Meng, K. Chen, X. Yang, T. Wang, P. Sun, F. Liu, X. Yan, K. Shimano and G. Lu, High sensitivity and low detection limit of acetone sensor based on NiO/ $\text{Zn}_2\text{SnO}_4$  p–n heterojunction octahedrons, *Sens. Actuators, B*, 2021, **339**, 129912–129923.

